Estuaries and Coasts
https://doi.org/10.1007/s12237-021-00991-6

Seasonal Changes of Estuarine Gravitational Circulation: Response to the Annual Temperature Change

Shiho Kobayashi[1] · Kentaro Nagao[2] · Daiki Tsurushima[2] · Satoshi Sasakura[3] · Tateki Fujiwara[3,4]

Received: 23 September 2020 / Revised: 5 August 2021 / Accepted: 9 August 2021

Abstract

Estuarine circulation is a vertical circulation that develops along the salinity gradient in estuaries and nearshore coastal waters. Fresher, and therefore less-dense, water flows out of the estuary in the surface layer, while a deeper inflow brings water from the open sea into the estuary. This study uses 7 years of in situ current measurements and hydrographic surveys to verify that this deeper inflow has two modes: a deep inflow that intrudes along the seabed, and a shallow-inflow that penetrates into the subsurface layer. These modes show seasonal variability, i.e., the deep-inflow mode occupies almost all of the winter season, whereas the shallow-inflow mode dominates during the summer. This mode change may play a key role in oxygen and carbon dioxide (CO_2) dynamics in estuaries and nearshore coastal waters. When the transition from deep- to shallow-inflow begins in spring, a cold water mass forms on the seabed in the upper estuary. This cold water mass is isolated from heating sources and oxygenated water; consequently, the cold water mass becomes hypoxic and accumulates both inorganic nutrients and CO_2 during spring and summer. When the transition from the shallow- to deep-inflow occurs, the CO_2, which is trapped in the bottom-water, is emitted to the atmosphere. The mechanism that causes the seasonal mode change in estuarine circulation is driven by the spatial inhomogeneity in the heating or cooling of the lower layer, which generates a horizontal density gradient in the layer. This mechanism highlights the importance of temperature in estuarine dynamics, which has not been extensively studied previously.

Keywords Estuarine circulation · Temperature · Inflow depth · Hypoxia · Carbon dynamics · Ise Bay

Key Points

- The seasonal change in the depths of the seawater inflow associated with estuarine gravitational circulation is elucidated using 7 years of in situ current measurements.
- Spatial inhomogeneity in heating or cooling in the lower layer causes a horizontal density gradient in this layer, and this induces the seasonal change in the inflow depth.
- The change in the inflow depth plays an important role in oxygen and CO_2 dynamics in estuaries and nearshore coastal waters.

Communicated by Neil Kamal Ganju

✉ Shiho Kobayashi
kobayashi.shiho.2z@kyoto-u.ac.jp

[1] Field Science Education and Research Center, Kyoto University, Oiwake-cho, Kitashirakawa, Sakyo-ku, Kyoto 606-8502, Japan

[2] Institute of Environmental Informatics, IDEA Consultants, Inc, 2-2-2 Hayabuchi, Tsuzuki-ku, Yokohama City, Kanagawa 224-0025, Japan

[3] Osaka Branch Office, IDEA Consultants Inc., 1-24-22 Nanko-kita, Suminoe-ku, Osaka City, Osaka 559-8519, Japan

[4] Kyoto University, Kyoto, Japan

Introduction

In coastal embayments that receive considerable inputs of freshwater, the horizontal salinity gradient is sufficient to generate a significant outgoing surface flux together with a compensatory inflow in the subsurface layer, and this is known as estuarine circulation (Pritchard 1952). The estuarine circulation is the sum of the gravitational circulation, the tidal residual circulation, and the circulation induced by asymmetric tidal mixing (Valle-Levinson 2011). The main topic of this study is the component of the gravitational circulation. The compensatory inflow has multiple patterns; e.g., bottom inflow associated with two-layered vertical circulation, intermedium inflow associated with three-layered circulation (Banas et al. 2004; Thomson et al. 2007), and surface inflow associated with reverse estuarine circulation (Giddings and MacCready 2017).

The driving force of bottom-water inflow associated with two-layered vertical circulation is the horizontal density gradient (Pritchard 1956; Hansen and Rattray 1966). In

an estuary that has a sill, the intrusion depth changes over the neap–spring tidal cycle (i.e., increasing salinity coincides with deeper intrusions, whereas decreasing salinity leads to intermediate intrusions and a three-layered structure) (Thomson et al. 2007; Geyer and MacCready 2014; Belzile et al. 2016). Estuarine circulation structure is not only affected by bathymetry (e.g., sills), but also morphology. Both modify the momentum balance through nonlinear advection and stress divergence (Lerczak and Geyer, 2004; Basdurak and ValleLevinson, 2012). Tidal variability of stress divergence and its interaction with horizontal density gradients contribute to estuarine circulation at subtidal temporal scales (Valle-Levinson 2011). Curvature (Chant 2002) and eddy viscosity-shear covariance (Cheng et al., 2019; Dijkstra et al., 2017), which includes tidal straining (Burchard and Hetland, 2010), can also affect estuarine circulation flows.

Local and remote wind forcing can cause surface inflow associated with reverse estuarine circulation or intermediate inflow associated with the three-layered residual flow (Hickey 2002; Giddings and MacCready 2017). The seasonal variability of estuarine circulation associated with salinity has also been measured in many estuaries (Nidzieko and Monismith 2013; Conroy et al. 2020). These studies noted the roles of wind forcing or salinity changes in controlling the depths of compensatory inflow associated with estuarine circulation.

In this study, we focused on the role of seasonal changes in water temperature on affecting the depths of compensatory inflow in a temperate estuary, where the water temperature fluctuates seasonally and freshwater flows into the estuary head. In this study, we defined upper and lower layers that are above and below the pycnocline in the stratified region. The lower layer is further divided into intermediate and bottom layers, which are above and below the top of the cold water mass, which has previously been referred to as the cold water pool, cold water cushion, or cold dome (Hill 1993; Houghton et al. 1982), and is formed in a heating period. These boundary lines are extended horizontally to allow their use in weakly stratified and strongly mixed regions and are also applied to the cooling period.

Changes in the depth of the compensatory inflow can influence the vertical distribution of oxygen and CO_2. Stigebrandt and Kalén (2013) showed that high-salinity and dense water intrusion into the bottom of a fjord improved oxygen conditions in the bottom layer. Fujiwara and Yamada (2002) estimated the vertical profile of density flow from the longitudinal pressure gradient in Tokyo Bay. Based on their results, Fujiwara et al. (2002) showed that the hypoxic bottom-water mass, which corresponded to a cold bottom-water mass rich in inorganic nutrients and CO_2, appeared in the bottom layer when the depth of the estuarine compensatory inflow was in the intermediate layer. However, the cold bottom-water mass rose and disappeared when the depth of the estuarine compensatory inflow was in the bottom layer. The compensatory inflow was then entrained into the surface water and carries materials trapped in the lower layer, such as inorganic nutrients and CO_2.

The surface outflow associated with estuarine circulation has been measured in previous studies (e.g., Hickey 2002; Guo and Valle-Levinson 2007; Kobayashi et al. 2010; Dzwonkowski et al. 2011), and the estuarine compensatory inflow has been studied using the salinity balance and isohaline coordinate analysis based on monthly results (e.g., MacCready 2011; Chen et al. 2012; Wang and Geyer 2018; MacCready et al. 2018). However, direct measurements of the vertical structure of the velocity over a period of several years is not sufficient for analysis of the seasonal changes in the depths of the estuarine compensatory inflow, which has an important role in controlling nutrient, oxygen, and CO_2 dynamics in estuaries and coastal seas (Chen and Borges 2009; Shearman and Brink 2010).

In this study, our working hypotheses were as follows. (1) Although the seawater density σ is generally governed by the salinity S in the estuary, the temperature change ($\partial T/\partial t$) is the main control on seasonal density changes ($\partial\sigma/\partial t$) in the lower layer defined above, where T is temperature, and t is time. (2) The temperature in the lower layer increases or decreases faster around the estuary mouth than around the estuary head, because there is generally strong salinity stratification around the estuary head, which prevents heat transfer from the surface to deeper waters. (3) Spatial heterogeneity of heating or cooling in the lower layer causes a seasonal change in the horizontal density gradient in this layer. If the density of the lower layer around the estuary mouth is larger than around the estuary head, then the depth of the compensatory inflow is generally in the bottom layer. However, if it is smaller than around the estuary head, then the depth of the compensatory inflow may possibly change from the bottom to the intermediate layer.

In this study, we analyzed seasonal changes in the depth of the compensatory inflow using velocity data obtained by continuous measurements for 7 years in the coastal plain estuary of Ise Bay, Japan (Fig. 1). We examined the mechanisms that could induce seasonal changes of inflow depth. As such, we tested working hypotheses (1) to (3) with observational data. Firstly, we investigated the effect of the temperature change ($\partial T/\partial t$) on the seasonal density change ($\partial\sigma/\partial t$) in the lower layer. Secondly, we examined the along-estuary variability of the timing when the temperature in the lower layer increased and decreased due to heating or cooling. Finally, we investigated the seasonal changes in the along-estuary horizontal density gradient in the lower layer. We also discuss the influences of changing inflow depth on hypoxic conditions and accumulation and transport of CO_2.

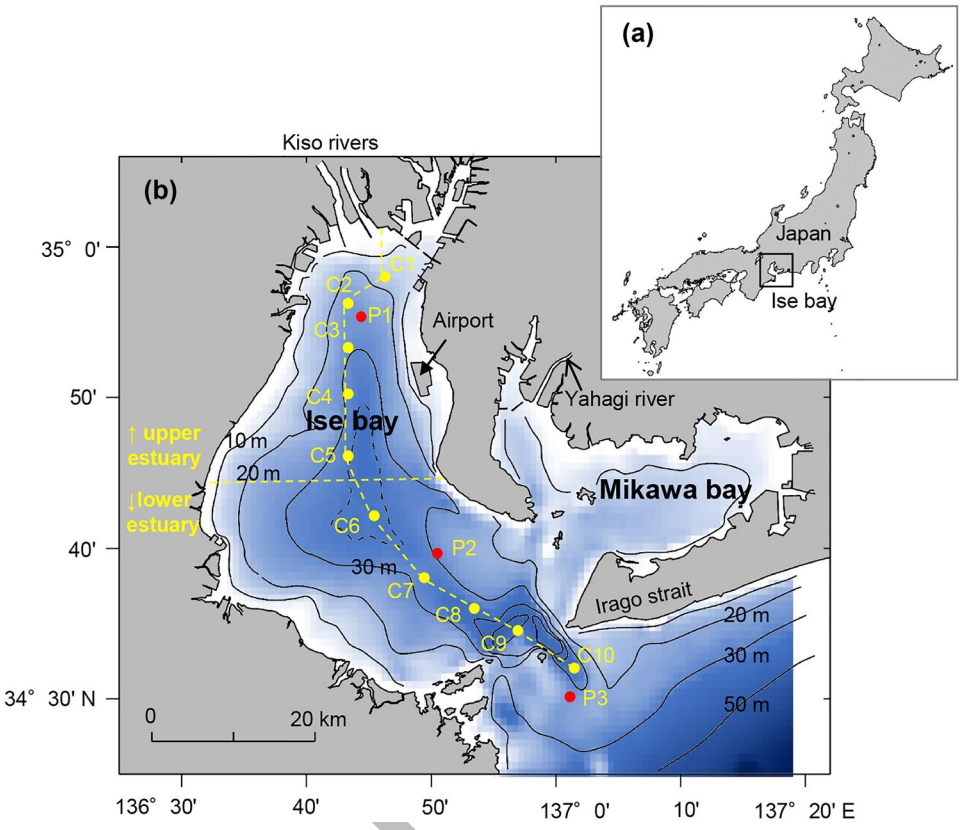

Fig. 1 **a** Location of Ise Bay. **b** Map of Ise Bay and the station locations. Yellow circles are stations used for repeated hydrographic observations by the Japan Coast Guard. Red circles are monitoring posts for continuous measurements of the vertical profiles of water temperature, salinity, dissolved oxygen, flow direction and velocity, and wind direction and speed. The dotted yellow line that links stations C1–10 shows the major axis of the bay. The other dotted yellow line perpendicular to the major axis defines the upper and lower estuaries

Materials and Methods

Description of the Study Area

The coastal embayments along the southern coast of Japan, which receive considerable inputs of freshwater, provide an opportunity to study estuarine gravitational circulation. Thus, we refer to these embayments as *estuaries*. Each estuary has a major freshwater source at its head, and the freshwater input is the driving force of the gravitational circulation in the estuaries.

The study site is Ise Bay, which is a coastal plain estuary located on the southern coast of Japan (Fig. 1). Three major rivers, known collectively as the Kiso rivers, flow into the bay head in the north. The bay opens into the Pacific Ocean to the south through Irago Strait (i.e., the bay mouth). The relatively shallow side of the embayment is Mikawa Bay (average depth = 9.2 m), which is located on the southeast side of Ise Bay. Ise Bay has a mean depth of 19.5 m, surface area of 1738 km^2, and volume of 33.9 km^3 (Coastal Oceanography Research Committee 1985).

River runoff is the main source of freshwater to Ise Bay. Surface precipitation and evaporation are an order of magnitude smaller than the total riverine discharge (Fig. 2b). The discharge from the Kiso rivers varies between a minimum of 208 $m^3\ s^{-1}$ in winter to a peak of 958 $m^3\ s^{-1}$ in summer, with an annual mean of 470 $m^3\ s^{-1}$ (Fujiwara et al. 2002). There is also river runoff into Mikawa Bay that is connected to Ise Bay. The annual mean discharge from Yahagi River to Mikawa Bay is 42 $m^3\ s^{-1}$ (in 2019; URL1), which is an order of magnitude smaller than the discharge from the Kiso rivers.

The tides in Ise Bay are dominated by semi-diurnal constituents. The amplitude of the tide ranges from 0.80 m at the bay mouth to 0.95 m at the bay head for the spring tide and from 0.29 to 0.34 m for the neap tide (URL2). The typical tidal current speed is 0.1 m s^{-1} inside the bay, whereas it exceeds 0.8 m s^{-1} during spring tides around the bay mouth (Fujiwara et al., 2002), because of the narrow strait (Fig. 1b).

In this study, we define the northern half of Ise Bay (i.e., north of the line between stations C5 and C6: Fig. 1b) as the upper estuary, while the southern half of the bay is the lower estuary. We define the regions around stations P1 and C9 (Fig. 1b) as the estuary head and mouth, respectively.

Data Collection

The data used in this study are listed in Table 1. Monthly hydrographic surveys have been carried out from 2010 to 2019 by the Japan Coast Guard using a conductivity–temperature–depth (CTD) profiler (RINKO Profiler ASTD153; JFE Advantech) along a longitudinal section of Ise Bay. The locations of these

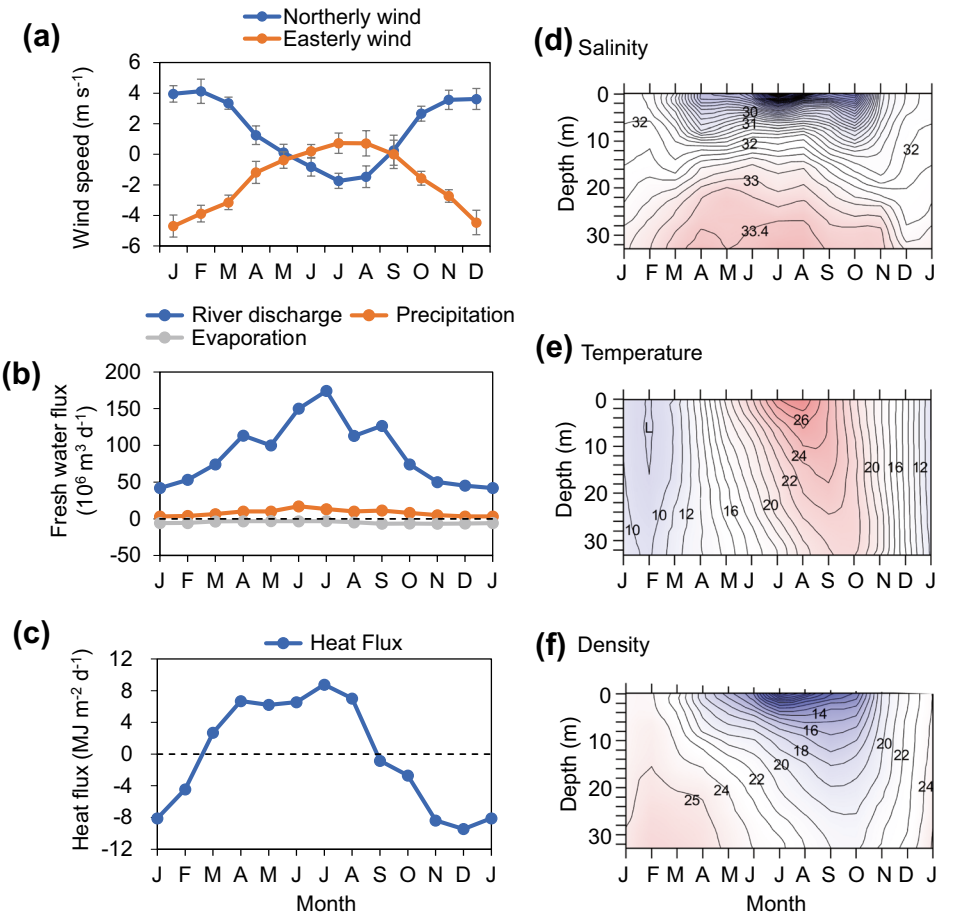

Fig. 2 **a** Climatological values of monthly mean northerly and easterly wind speeds (m s^{-1}; vector mean) measured at the maritime airport (Fig. 1b) averaged over the period from 2010 to 2019. Negative and positive values indicate northward and southward winds, respectively. Bars in each figure show the standard deviations. Climatological values of **b** freshwater flux (10^6 m^3 day^{-1}) and **c** heat flux (MJ m^{-2} day^{-1}) in Ise Bay, which were taken from the publication by the Coastal Oceanography Research Committee (1985). Seasonal variations of the vertical profiles of **d** salinity, **e** temperature (˚C), and **f** density observed at station C5 (Fig. 1b). The contour intervals of **d**–**f** are 0.2, 1.0 °C, and 1.0 kg m^{-3}, respectively. The monthly values were obtained by averaging the results of the monthly observations from 2010 to 2019

stations are shown in Fig. 1b. The longitudinal section of the bay was taken along its deepest points starting from the bay head (stations C1–10: Fig. 1b). The dataset is openly available on the internet (URL3). In this study, we used temperature, salinity, and dissolved oxygen (DO) data at 1-m intervals from the surface to seafloor, which was obtained by averaging of the 0.1-m interval data and the calculated density.

The Mie Prefecture Fisheries Research Institute has also been conducting similar monthly hydrographic surveys using a CTD profiler (RINKO Profiler ASTD153; JFE Advantech) at 15 stations, which cover all of Ise Bay. The dataset is openly available on the internet (URL4). In this study, we used the DO, salinity, and pH (NBS scale) data for water 1 m above the seafloor, in order to obtain the concentrations of carbon species. The data from July 2019 were used in this study.

The Nagoya Research and Engineering Office for Port and Airport, Chubu Regional Development Bureau, Ministry of Land, Infrastructure, Transport, and Tourism, Japan, installed a real-time monitoring system that has been operating continuously from 2010 to 2016 at three stations in Ise Bay. The locations of stations P1, P2, and P3 are shown in Fig. 1b, and the water depths at these stations are 28.0, 30.0, and 30.1 m from the mean sea level, respectively. The dataset is openly available on the internet (URL5). The hydrographic data are measured every hour using automatically elevating CTD profilers (JFE Advantech) from the surface to the seafloor at 1-m intervals at P1 and P2. The vertical profiles of the horizontal currents at P2 have been measured using a bottom-mounted acoustic Doppler current profiler (ADCP; AWAC, Nortek AS), as described in detail in the next section. The ADCP has three beam transducers directed at 25° from the vertical. The sampling rate, ensemble averaging, and data analysis depths and intervals are listed in Table 1. Vertical profiles of the flow, temperature, and salinity were not obtained at P3, because the observation equipment was fixed at three layers.

Hourly wind speeds are recorded at Chubu Airport, which is located over the sea (Fig. 1b), by the Japan Meteorological Agency, and are published online (URL6). The data from 2010 to 2019 were used in this study. The freshwater flux (10^6 m^3 day^{-1}) and heat flux (MJ m^{-2} day^{-1}) for Ise Bay were taken from the publication by the Coastal Oceanography Research Committee (1985).

Table 1 List of analysis data

Current mooring measurement at station P2	
Water depth	30.0 m from mean sea level
Research institution	Ministry of Land, Infrastructure, Transport and Tourism, Japan
Instrument	Bottom-mounted ADCP(AWAC, Nortek AS)
Sampling rate (pings)	1 Hz
Ensemble averaging	1-min simple average
Analysis data	30-min interval data
Data analysis period	Feb. 2010–Mar. 2016
Data analysis depths	2-m depth interval from 6.5 to 24.5 m
Data used for	Figure 6
CTD mooring measurement at station P1 and P2	
Water depth	28.0 m (P1), 30.0 m (P2) from mean sea level
Research institution	Ministry of Land, Infrastructure, Transport and Tourism, Japan
Instrument	CTD profilers (Automatic elevating system, JFE Advantech)
Sampling time interval	Every 1 h
Sampling depth interval	1-m depth interval
Analyzed item	Water temperature and salinity
Data analysis period	Feb. 2010–Mar. 2016
Data analysis depths	From surface to 1 m and 4 m above the bottom at P1 and P2
Data used for	Figures 5 and 8
CTD ship cruise measurement at station C1 to C10	
Research institution	Japan Coast Guard
Instrument	CTD profiler (RINKO Profiler ASTD153, JFE Advantech)
Sampling time interval	Every 1 month
Sampling depth interval	0.1-m depth interval
Data analysis interval	1-m depth interval extracted from raw data
Analyzed item	Water temperature, salinity and dissolved oxygen
Data analysis period	Feb. 2010–Dec. 2019
Data analysis depths	From surface to 1 m above the bottom
Data used for	Figures 2c, d, e; 3; 4; and 7
CTD ship cruise measurement covering the whole of the Bay	
Research institution	Mie Prefecture Fisheries Research Institute
Instrument	CTD profiler (RINKO Profiler ASTD153, JFE Advantech)
Number of stations	15 stations
Analyzed item	water temperature, salinity, dissolved oxygen and pH (NBS scale)
Data analysis period	Jul. 2019
Data analysis depths	1 m above the bottom
Data used for	Figure 10

Data Analysis

Temperature, salinity, and DO data at 1-m intervals from the surface to the seafloor were obtained by averaging 0.1-m interval data obtained by the Japan Coast Guard. Density was obtained from temperature and salinity data of UNESCO (1983). Monthly temperature, salinity, and density data were obtained by averaging the 2010–2019 data at each station.

The Brunt–Väisara frequency at 1-m intervals was calculated using monthly density data obtained by averaging from 2010 to 2019 at stations C3, C5, and C9 (Fig. 1b). The frequency shows the along-estuary variability of buoyancy characteristics.

Vertical profiles of the horizontal currents from 2010 to 2016 at P2 (30.0 m depth) were obtained from the real-time monitoring system at 30-min intervals at a depth range of 6.5–24.5 m below the mean sea level. The velocity data were

obtained in 2-m depth intervals, and the data from the surface to 6.5 m depth and from the seafloor to 24.5 m depth were excluded because it was affected by side lobe effects.

Tidal components were removed from the velocity data for each component and depth using a harmonic analysis method with the semi-diurnal and diurnal tidal constituents (M_2, S_2, K_1, and O_1) and overtide constituents (M_4, MS_4, and M_6). A harmonic analysis was conducted on the data for each year from 2010 to 2016. The obtained residual currents were averaged for 24 h and used as the daily mean residual currents. Hereafter, we refer to this as the residual current. The residual currents were resolved into two orthogonal directions: up-estuary (315° from north) and cross-estuary (45° from north).

Hourly wind speeds from 2010 to 2019 were converted into northerly and easterly components, and each component was averaged monthly. From the monthly wind vectors obtained for 10 years, the climatological mean wind speed and its standard deviation were calculated for each month.

The Driving Force of the Density Current

The baroclinic pressure gradient is calculated using measured density, as following the previous study in Tokyo bay (Fujiwara and Yamada 2002). Ise bay has common geographic features with Tokyo bay, where main rivers flow into the bay head in the north, and the bay opens into the ocean to the south through the strait.

Fujiwara and Yamada (2002) used a balance between the pressure gradient force and vertical frictional force:

$$P(x,z) = g\rho_0\eta(x) + g\int_0^z \rho\left(x,z'\right)dz' \tag{1}$$

Here, P, g, η, ρ, and ρ_0 are pressure (N m^{-2}), gravitational acceleration (m s^{-2}), sea level height (m), seawater density, and surface water density (kg m^{-3}), respectively; z is the axis point vertically downward from the sea surface (m), with positive values downward; x is the horizontal distance (m) between the stations.

Then, the driving force D ($=-\partial P/\partial x$) which was derived from Eq. 1 to

$$D = -\rho g\frac{\partial \eta}{\partial x} - g\int_0^z \frac{\partial \rho(z')}{\partial x}dz' \tag{2}$$

They are called the vertical average of the driving force and the deviation force D_m and D_d, respectively (Fujiwara and Yamada 2002):

$$D_m = \frac{1}{h}\int_0^h D\,dz \tag{3}$$

$$D_d = D - D_m \tag{4}$$

Considering the steady state, this term D_m becomes small because net circulation velocity $\int_0^h u\,dz$ is negligibly small in a channel that has a closed end (Fujiwara and Yamada 2002). Thus, the term D_d, can be obtained as driving force of the density current using mean density profiles at stations C5 and C9, which lie either side of station P2 (shown in Fig. 1b).

Calculation of Carbon Species Concentrations

In order to examine the influences of changing inflow depth on hypoxic conditions and accumulation of CO_2, the relationships between DO and the partial pressure of carbon dioxide (pCO_2), and DO and dissolved inorganic carbon (DIC), were analyzed using data measured by the Mie Prefecture Fisheries Research Institute.

The concentration of DIC and pCO_2 can be calculated from the *TA* estimated from salinity and pH measured by using CO2SYS, the program developed by Lewis and Wallace (1998).

In general, the total alkalinity of the seawater is closely correlated with salinity. The empirical relationship between salinity (S) and total alkalinity (TA) in Ise Bay was obtained using Eq. (5) (Taguchi and Fujiwara 2010):

$$TA\left(\mu mol\ kg - sw^{-1}\right) = S * 51.53 + 518 \tag{5}$$

(Correlation coefficient $R = 0.997, n = 159$)

The concentration of dissolved inorganic carbon (DIC) and partial pressure of carbon dioxide (pCO_2) in Ise Bay were calculated using *TA* estimated from salinity and pH measured 1 m above the bottom.

Results

Seasonal Changes in Meteorological and Hydrological Properties

The seasonal change in the heat flux is positive from March to August (i.e., the heating period), with a maximum value of 8.6 MJ m^{-2} day^{-1} in July (Fig. 2c). The heat flux becomes negative from September to February (i.e., the cooling period), with a minimum value of − 9.6 MJ m^{-2} day^{-1} in December (Fig. 2c). In this study, March–May, June–August, September–November, and December–February are defined as spring, summer, autumn, and winter, respectively. The river discharge increases from April to September, with a maximum value of 170×10^6 m^3 day^{-1} in July (Fig. 2b).

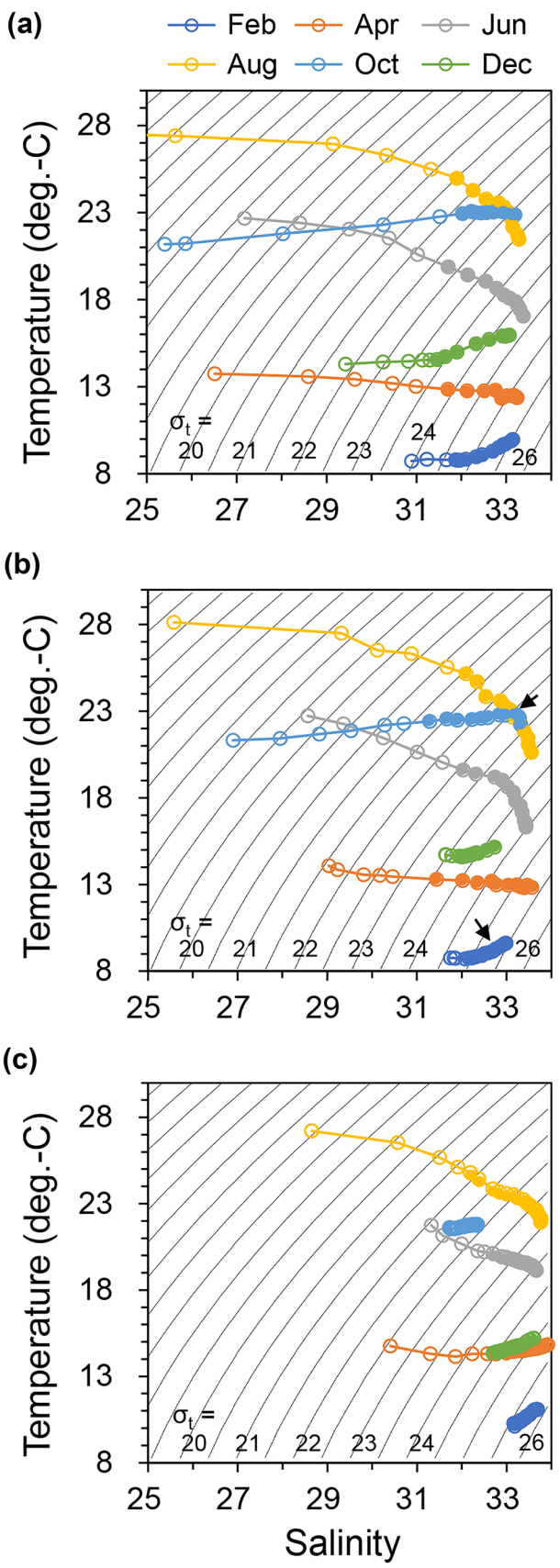

Fig. 3 Temperature–salinity diagram of the vertical profiles obtained every 2 months at stations **a** C3, **b** C5, and **c** C9 (2-m depth intervals; data are the same as Fig. 2d–f). Filled circles are data from deeper than 10 m. The arrows in **b** show the data at a depth of 20 m in February and August, which is described in detail in the text

The winds over Ise Bay show significant seasonal changes (Fig. 2a), with a northwesterly wind predominant from November to March, and a prevailing southeasterly wind and wind speed decrease with values of 0.3 to 1.8 m s^{-1} in summer. Wind speed decreases to a minimum value of nearly zero in May and September (Fig. 2a).

The monthly vertical distributions of salinity, temperature, and density along the center of the estuary (station C5; Hovmöller diagrams) are shown in Fig. 2d–f. Salinity in the upper layer (i.e., between the surface and 10 m depth) remained low from spring to autumn, with a minimum value of 22.4 in July, suggesting freshwater input (Fig. 2d). The vertical gradient of salinity increased and was largest in summer, but decreased after November and was smallest in winter (Fig. 2d).

The seasonal variation of monthly temperature differs markedly from that of salinity (Fig. 2d, e). The contour lines in the salinity diagram are approximately horizontal from April to October, whereas those in the temperature diagram are approximately vertical throughout the year (Fig. 2d, e). Surface temperatures increase from February to August, and then decrease from September. Temperature in the lower layer increased faster than near-surface temperatures during the early heating period (February–April), although the solar heating mostly affects the sea surface (Fig. 2e).

The seasonal variation of density is similar to that of salinity in the upper layer (0–10 m depth); however, it resembles temperature in the lower layer (20 m depth to seafloor) throughout the year (Fig. 2f). The linear relationships between the difference of salinity at the seafloor and at 20 m depth with that of density at the seafloor and at 20 m depth and the difference of temperature at the seafloor and at 20 m depth with that of density at the seafloor and at 20 m depth at station C5 were examined through a regression analysis. There was no relationship between the salinity and density differences, and the coefficient of determination between the temperature and density differences was 0.81. This suggests that the lower-layer density is mainly controlled by temperature.

Figure 3 shows a temperature–salinity (TS) diagram for the vertical profiles at stations C3, C5, and C9 at 2-m intervals. TS diagrams from spring to autumn at stations C3 and C5 indicate that the vertical density profile is mainly controlled by salinity (Fig. 3a, b). However, the TS data for the lower layer, which is deeper than 10 m, are widely distributed in a vertical direction, the seasonal density change correlates with the seasonal temperature change, and the

salinity is insignificant (Fig. 3a, b). The TS diagram for station C9, which is located furthest from the freshwater source and near the narrow strait, has a smaller vertical difference in density than at stations C3 and C5 (Fig. 3c).

At station C5, the temperature and salinity at a depth of 20 m (Fig. 3c) are 9.0 °C and 32.5 in February, respectively, and 23.1 °C and 33.1 in August, respectively (Fig. 3b). The temperature increase of 14.1 °C (from 9.0 to 23.1 °C) caused a density decrease of 3.1 kg m^{-3} and, in contrast, the salinity increase of 0.6 (from 32.5 to 33.1) caused a density increase of 0.4 kg m^{-3}. The density change caused by temperature is larger than that caused by salinity.

Seasonal Changes in Seawater Inflow to the Upper Estuary

The longitudinal distributions of the monthly DO, temperature, and salinity data are shown in Fig. 4 for April (spring), July (summer), October (autumn), and December (winter) in 2010. The longitudinal distribution of DO is shown in Fig. 4a, where hypoxic water is represented by water masses with DO < 4 mg L^{-1}. Given that the inflow water is generally well-oxygenated and oxygen is mainly consumed by bottom sediment, low DO values are a proxy for areas that are not affected by oxygenated inflow waters (Fujiwara et al. 2002).

In April and July, the hypoxic water mass gradually increases on the seafloor, and this water mass is closely correlated with the cold bottom-water mass (Fig. 4a, b). The cold water mass is isolated from seasonal heating by the pycnocline (Fujiwara et al. 2002). This feature is clearly evident in the April data in Fig. 4b. The warm seawater (T > 13 °C) in the southern part of the bay enters the middle layer of the northern part of the bay (depth ~ 20 m). The water under this intrusion layer corresponds to the colder and lower DO water mass (Fig. 4a, b).

The intrusion of water that is 0.4–1.2 °C warmer than the water above 10 m depth into the layer below 15 m depth in

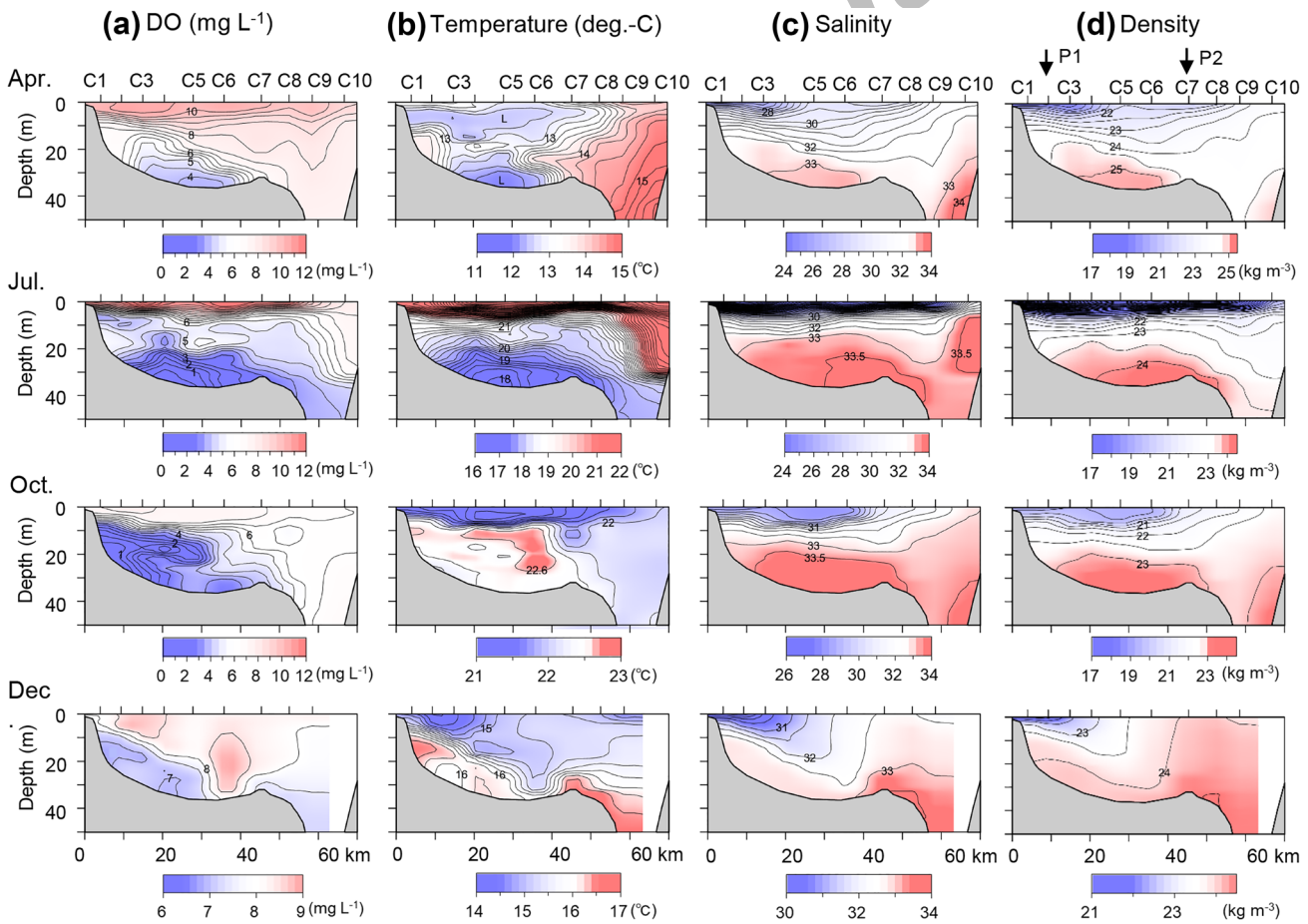

Fig. 4 Longitudinal distribution of **a** DO (mg L^{-1}), **b** temperature (˚C), **c** salinity and **d** density (sigma-t) obtained from monthly observations from April to December 2010. The contour intervals of **a**–**d** are 0.5 mg L^{-1}, 0.5 °C, 0.2, and 0.5 kg m^{-3}, respectively. The P1 and P2 arrows mark the positions of the mooring stations P1 and P2 (Fig. 1b), respectively. Stations C1 and C9 are associated with the estuary head and mouth, respectively

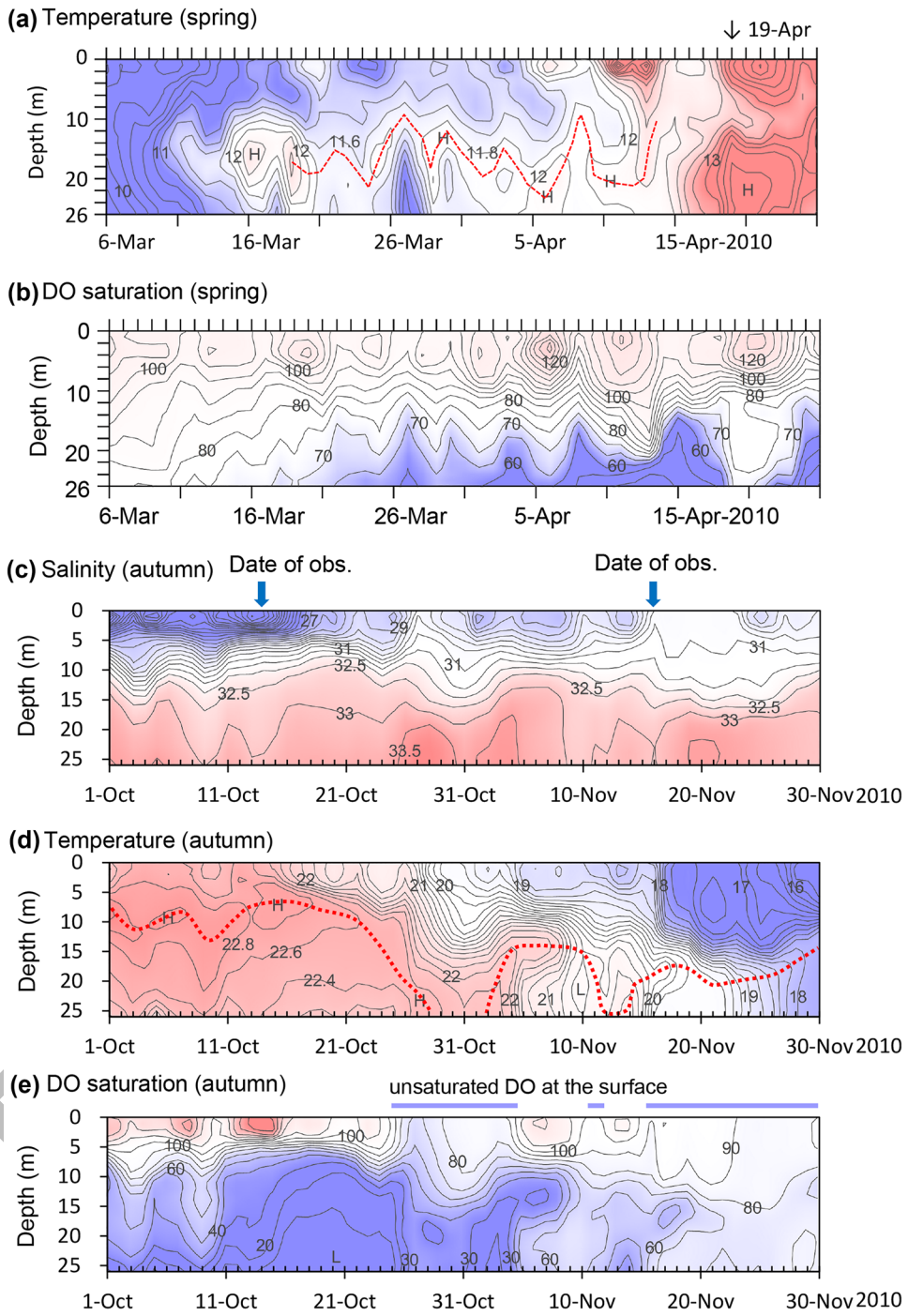

Fig. 5 Time-series of vertical profiles of **a** temperature and **b** DO saturation at station P1 in spring (6 March to 25 April 2010). Time-series of the vertical distribution of **c** salinity, **d** temperature, and **e** DO saturation recorded at station P1 in autumn (1 October to 30 November 2010). Red dotted lines in **a** and **d** represent the subsurface temperature maximum. Blue bars in **e** indicate the period when the surface DO is unsaturated. The contour intervals of **a**–**e** are 0.2 °C, 5%, 0.5, 0.2 °C, and 10%, respectively. *H* and *L* in **a** and **c** indicate "higher" and "lower" than surrounding values, respectively

April was identified from the continuous measurements at station P1, which is near station C2 (Fig. 5a, b). Although the vertical distribution of the water temperature was almost constant at 10 °C on 6 March, the water temperature in the middle layer (depth ~ 16 m) increased from 11 March, reaching 12.2 °C on 16 March. Subsequently, the middle layer continued to have the highest temperature (Fig. 5a), suggesting that seawater that was 0.4–1.2 °C warmer than the surface water above 10 m depth from the southern part of the bay flowed into the middle layer (Fig. 5a). Below this middle-layer inflow, the DO saturation gradually decreased, suggesting that bottom-water was stagnant and isolated from the inflow (Fig. 5b).

High-density water with a salinity of > 34 and temperature of 0.2˚C less than the middle layer was intruded from the lower to upper estuary on the seafloor, and then partially rose into the hypoxic water mass in October (Fig. 4). During the cooling period from October to December, the size of

the low-DO water mass gradually decreased, although the process was not a complete reversal of the heating season (Fig. 4a).

A prominent temperature change occurred in the cooling period (October–December: Fig. 4b). The bottom-water in the upper estuary became warmer than the lower estuary waters in October–December (Fig. 4b). Due to this change in the temperature distribution, the low-DO water corresponds to a cold water mass in the heating period, and then to water mass that is at least 1 °C warmer than the water in the middle layer in the cooling period (Fig. 4a, b).

The increased intrusion depth of seawater in autumn was also identified from the continuous measurements at station P1. Figure 5c, d, and e shows the time-series of vertical profiles of salinity, temperature, and DO saturation at station P1 from 1 October to 30 November 2010. The salinity gradually decreased above a depth of 10 m, but no noticeable change was observed below 10 m (Fig. 5c). The red dotted line in Fig. 5d represents the subsurface temperature maximum. The temperature above the red dotted line gradually decreases near the end of November and, below the line, it also decreases toward the seafloor. As such, the temperature around the red dotted line is the highest (Fig. 5d), which suggests the temperature decrease below the red line is not due to surface cooling. Water colder than the intermediate layer appeared on the seafloor on 6 and 18 November (Fig. 5d) and, on these dates, the DO concentrations on the seafloor (i.e., at 25 m depth) became higher than those at 15 m depth, suggesting the weakening of hypoxic conditions was not due to vertical mixing associated with surface cooling. The longitudinal DO and temperature distributions in Fig. 4a, b for October and December also show that water colder than the intermediate layer was distributed from the estuary mouth to head along the seafloor (Fig. 4b). Subsequently, DO on the seafloor increased and ascending hypoxic water formed a subsurface hypoxic water layer (Fig. 4a). In general, the hypoxic water mass that coincides with the bottom-water mass is at least 1 °C warmer than water in the middle layer (Fig. 5d, e) and is gradually eroded. The surface-water DO then becomes unsaturated (Fig. 5e).

Seasonal Changes in the Observed Velocity Profiles

Figure 6a shows the seasonal changes in the daily vertical profiles of the subtidal flows along the estuary measured at station P2. Low-salinity water was distributed from the surface to a depth of 12 m during the stratified season (Fig. 3a). At this time, it is possible to observe the estuarine gravitational outflow, although the ADCP data from the upper and lower 6.5 m were excluded from the analysis.

The depth and intensity of the maximum up-estuary flow were identified in a vertical profile of the daily mean subtidal flow. The daily inflow depth and maximum inflow velocity are shown in Fig. 6b and c, respectively. The thick black lines show the 15-day moving average, and the monthly averages of these values are presented in Fig. 6d and e, respectively, along with the standard deviations of the monthly mean values.

Two-layered flow was maintained from autumn to winter (September–February) and consisted of outflow in the upper layer and inflow in the lower layer (Fig. 6a). In 2010, the maximum inflow was located at a depth of 20 m in April, and then gradually moved upward to 6.5 m in July. Subsequently, the depth of maximum inflow descended back to 20 m by October (Fig. 6b). These seasonal changes in inflow depth (i.e., ascending and descending during the heating and cooling periods, respectively) can be clearly observed in the data from 2010, 2011, 2013, and 2015. In other years, the seasonal change is not as well defined, but a similar tendency is evident (Fig. 6b).

In the years during which the seasonal variation is well defined in Fig. 6a, the inflow depth shows prominent seasonal changes (Fig. 6 b and d). However, in other years (e.g., 2012 and 2014), the summer peak splits into multiple peaks. Figure 6 d shows that the inflow depth increases from January, reaches a peak in August, and then rapidly decreases through to December. The inflow depth fluctuates significantly in summer but less so in winter. The maximum inflow velocity was 7.9 ± 1.9 cm s^{-1} in July and 5.5–6.8 cm s^{-1} from November–March (Fig. 6c and e).

Driving Force of the Seawater Inflow to the Upper Estuary

To investigate the mechanisms of seawater inflow into the upper estuary, we calculated the driving force of the density current between stations C5 and C9, which lie either side of station P2 (i.e., the ADCP station). Figure 7 a, b, c, and d show the salinity, temperature, density, and pressure gradient between stations C5 and C9, respectively. The salinity difference ($\Delta salinity$ = salinity at C5—salinity at C9) is negative all year in the upper layer, and the difference increases from −1.4 in spring to −4.8 in autumn, whereas the salinity difference is small (−0.2 to 0.0) in the lower layer (Fig. 7a).

The temperature difference shows a prominent seasonal pattern (Fig. 7b). In the heating period, the temperature in the lower layer in the upper estuary (station C5) is about 3 °C lower than in the lower estuary (station C9) (Fig. 7b), which is consistent with the presence of a cold water mass at station C5 (Fig. 4b). This temperature difference causes the bottom-water in the upper estuary to be dense, with a maximum density difference of 0.6 kg m^{-3} during the heating period (Fig. 7c). In the cooling period, the temperature in the lower layer at station C5 is about 1.5 °C higher than at station C9 (Fig. 7b). Thus, in the lower layer, the temperature

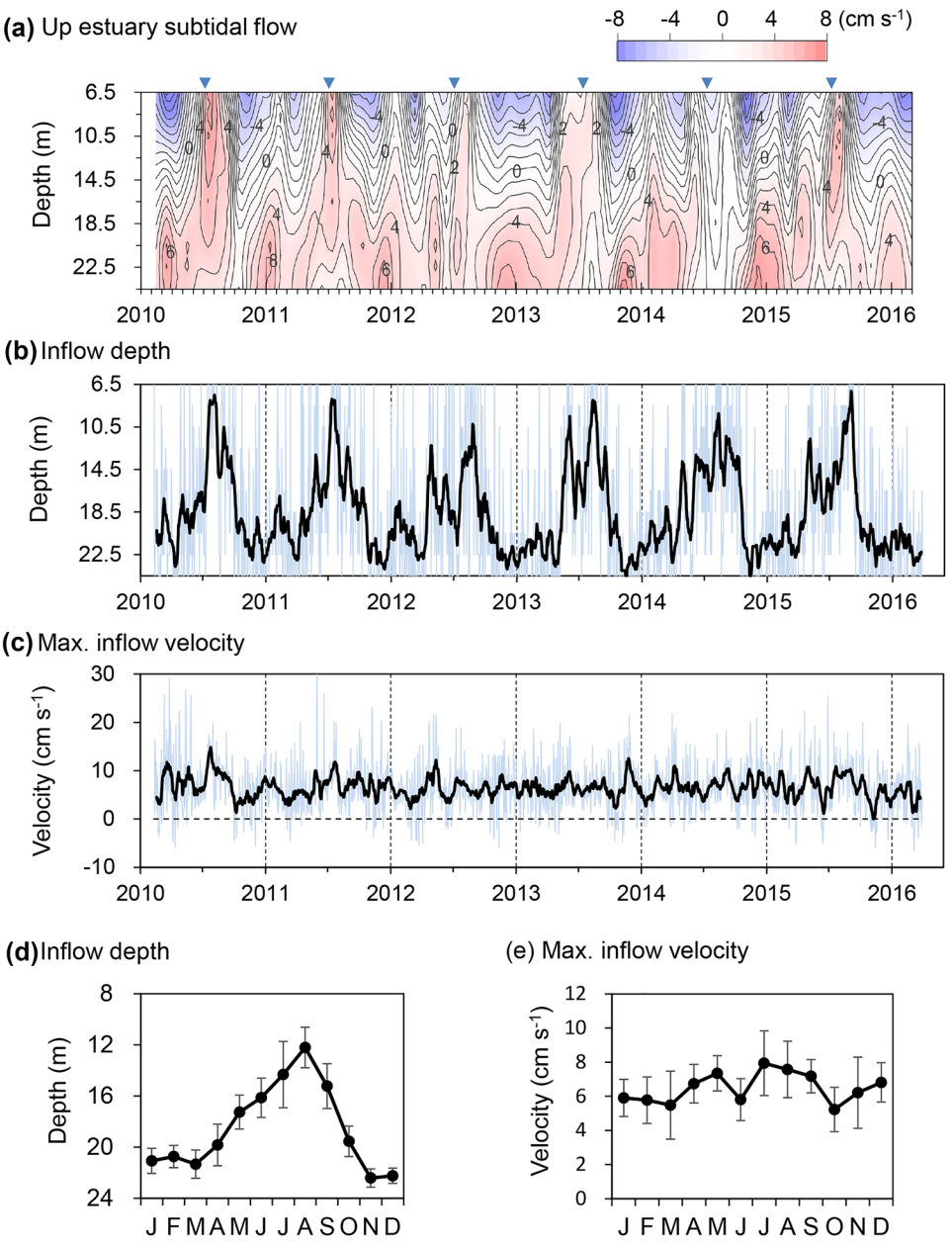

Fig. 6 **a** Up-estuary subtidal flow (cm s^{-1}) from February 2010 to March 2016 at station P2, where the water depth is 30 m. Inverted triangles indicate July. **b** Inflow depth and **c** maximum inflow velocity. Thin and thick lines show the daily values and 15-day moving averages, respectively. Monthly average values of **d** inflow depth and **e** maximum inflow velocity. Error bars represent the standard deviations of the monthly mean values

increase and decrease in the lower estuary are more rapid than in the upper estuary.

The positive driving force in Fig. 7d represents the force required to push the seawater toward the upper estuary. This force reaches a maximum on the seafloor from November to February in winter, but increases in the intermediate layer from April to September. A heavier water mass exists from April to September on the seafloor in the upper estuary (station C5: Fig. 7c), which is consistent with the change in the depth of the inward force to the intermediate layer. After temporarily weakening in August, the maximum inward force descends to the seafloor in October (Fig. 7d). This seasonal change in the depths of the maximum inward force is similar to that of the inflow depth indicated by the measured flow (Fig. 6d).

The seasonal changes in the vertical profiles of the Brunt–Väisara frequency (N^2) at stations C3 (uppermost estuary), C5 (upper estuary), and C9 (lower estuary) are shown in Fig. 8a-c. Seasonal changes in the degree of stratification were common at all stations, while in the cooling period, N^2 at station C3 was larger than those at stations C5 and C9, where N^2 was nearly zero. At depths above 5 m, N^2 at station C3 was strongly affected by freshwater input and larger than at the other stations. In contrast, at depths below 5 m, N^2 at stations C3 and C5 was larger than at station C9 (Fig. 8a-c).

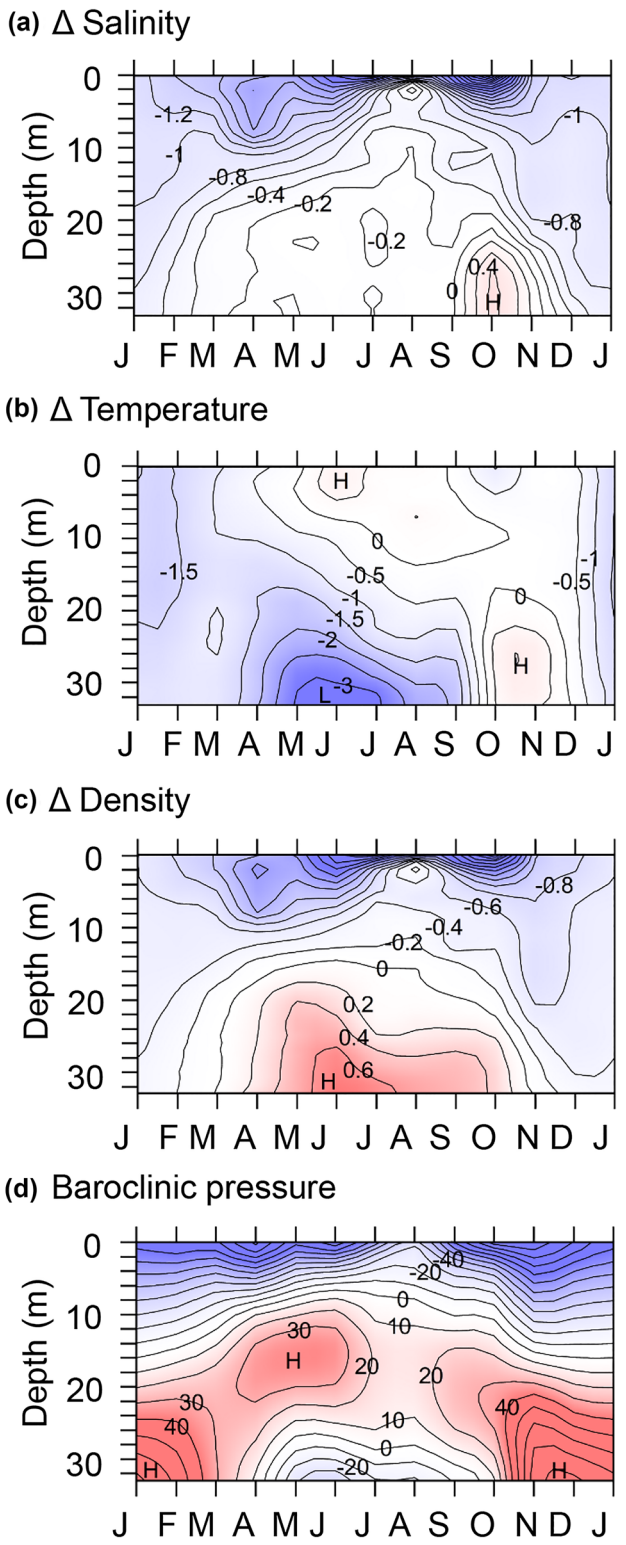

Fig. 7 Seasonal changes in **a** salinity, **b** temperature (°C), and **c** density (kg m^{-3}), and the differences between stations C5 and C9 (Fig. 1b) averaged over the period from 2011 to 2017. **d** Baroclinic pressure difference (N m^{-2}) between stations C5 and C9 calculated using the data shown in Fig. 7c. The contour intervals of **a**–**d** are 0.2 °C, 0.5, 0.2 kg m^{-3}, and 10 N m^{-2}

The temperature difference between the uppermost and upper estuary (i.e., stations C3 and C5) and the upper and lower estuary (i.e., stations C5 and C9) is shown in Fig. 8d, e. The depths at 5 and 25 m are representative of the upper and lower layers, respectively. In the lower layer, the temperature in the lower estuary (station C9) increases faster than that in the uppermost and upper estuary (stations C3 and C5) during the heating season (Fig. 8d, e). During the cooling period, the temperature decreases more rapidly in the lower estuary (station C9) than in the uppermost and upper estuary (stations C3 and C5) (Fig. 8d, e). The temperature difference between the uppermost estuary (station C3) and upper estuary (station C5) also showed seasonal changes, while the temperature difference in the heating season was smaller than that between the upper and lower estuary (stations C5 and C9) (Fig. 8d). This difference in response is responsible for the difference in the strength of stratification between the upper and uppermost estuary and lower estuary in the lower layer (Fig. 8a-c).

Discussion

Effect of Annual Temperature Changes on the Estuarine Gravitational Circulation

Estuarine circulation is a vertical circulation that develops along the salinity gradient in estuaries and nearshore coastal seas. Fresher and less dense water flows out of the estuary in the surface layer, while a deeper inflow brings water from the open sea into the estuary. In this study, we used in situ current measurements and hydrographic surveys covering a period of 7 years to verify that the deeper inflow associated with estuarine circulation has two modes: a deep inflow intruding along the seafloor (Fig. 9b) and a shallow inflow penetrating into the subsurface layer (Fig. 9a). These modes exhibit seasonality changes, whereby the deep inflow mode dominates through almost all of winter and the shallow inflow mode dominates during summer (Figs. 5 and 6).

Buoyancy is caused by freshwater inflow and surface heating during the heating period from March to August (Fig. 2c). In contrast, the buoyancy associated with freshwater inflow is counteracted by surface cooling during the cooling period from September to February (Fig. 2c). The buoyancy loss is greater in winter (Fujiwara et al. 2002). For example, in December, the buoyancy loss caused by cooling was estimated to be 7.2×10^{-8} m^2 s^{-3}, while the buoyancy supplied by the freshwater flux per unit area, which was obtained by dividing the river discharge by the surface area of the bay in the same month, was 2.9×10^{-8} m^2 s^{-3} (Fujiwara et al. 2002).

In April and July, the hypoxic water mass gradually increased in size on the seafloor, and this water mass is

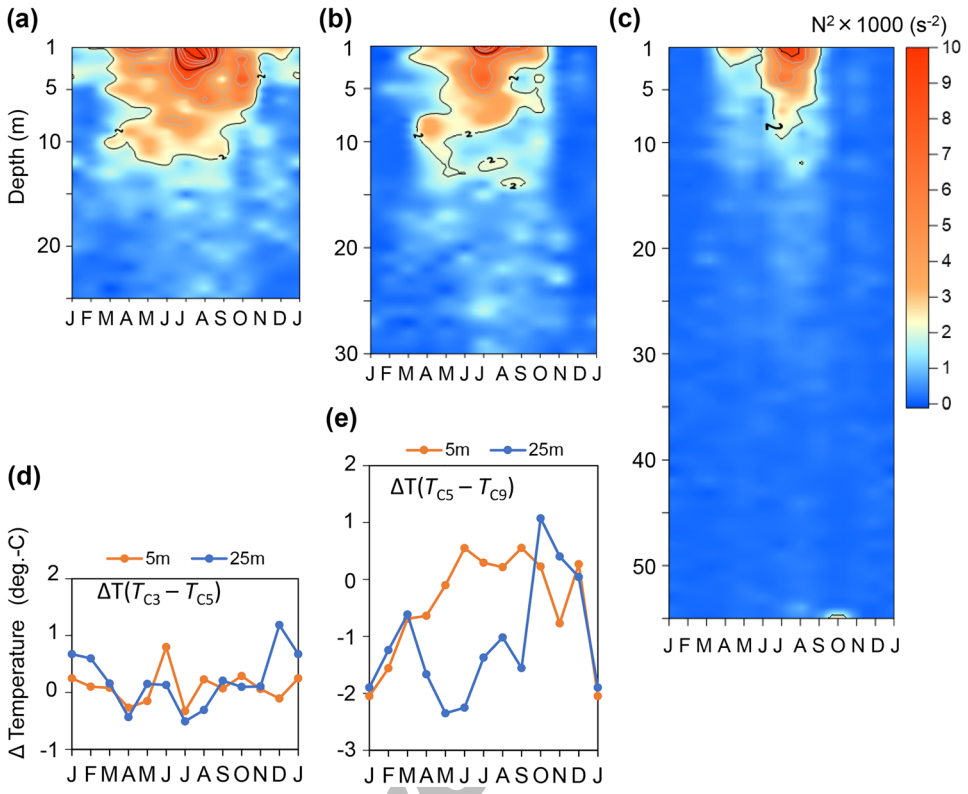

Fig. 8 Seasonal changes in the vertical distributions of the Brunt–Väisara frequency ($\times 1000\ s^{-2}$) at stations **a** C3, **b** C5, and **c** C9 (Fig. 1b). Seasonal changes in temperature differences between stations (**d**) C3 and C5 (=TC3 − TC5) and (**e**) C5 and C9 (=TC5 − TC9) at 5 and 25 m depths. The monthly mean values were calculated using the monthly observations from 2010 to 2016

closely correlated with the cold bottom-water mass (Fig. 4a, b). These features indicate that the inflow current does not pass directly above the seafloor, but flows in the intermediate layer at some distance above the seafloor (Fig. 6a). In contrast, the low-DO bottom-water mass was eroded during the cooling period (October–December: Fig. 4), suggesting that the inflow depth of saline, cold, and heavy water deepened gradually. Previous studies have identified seasonal changes in the distributions of low-DO and cold water masses in semi-enclosed embayments with similar geographical features to Ise Bay, such as Tokyo Bay (Fujiwara and Yamada 2002), Osaka Bay (Nakajima and Fujiwara et al. 2007), and Sakai Hama (Fujii et al. 2015). The seasonal changes in inflow depth are observed in coastal embayments that have a freshwater source at their estuary head, a strongly stratified upper estuary, and a weakly stratified lower estuary.

Effects of Wind, River Advection, Earth Rotation, and Bathymetry on the Inflow Depth

Wind stress variations may enhance, invert, or dampen estuarine gravitational circulation (Reyes-Hernandez and Valle-Levinson 2010). At the study site, the winter and summer monsoon winds are northwesterly and southeasterly, respectively, and the wind speed in winter is larger than that in summer (Fig. 2a). The wind stress can be estimated following the method of Large and Pond (1981):

$$\tau_s = \rho CD|U_{10}|U_{10}\left(4.0 \leqq U_{10} < 11.0\right),$$

where U_{10} is the wind speed at 10 m above the sea surface, ρ is the atmospheric density at 20 °C (1.2043), and CD is the bulk coefficient (1.2×10^{-3}). The maximum U_{10} in the study area is 3.8 m s^{-1} in summer and 7.9 m s^{-1} in winter (Fig. 2a), and the wind stress is estimated to be 0.02 N m^{-2} in summer and 0.09 N m^{-2} in winter.

Assuming the average depth of the deep channel H_0 is 25 m and the eddy viscosity A_z is 0.025 $m^2\ s^{-1}$, the scale of the residual current driven by the local wind U_r is $2.5\times\tau_s$, and a 0.1 N m^{-2} wind stress will drive a residual current of the order of 2.5 cm s^{-1} (Wong 1994). In winter, the wind stress in Ise Bay with an average depth of the deep channel H_0 of 30 m is 0.09 N m^{-2}, and thus, the typical magnitude of the wind-driven current is 2.7 cm s^{-1}. The estuarine gravitational flow expected from the horizontal density gradient in winter is two-layered exchange flow (Fig. 7) and, therefore, the northwesterly wind in winter does not affect the inflow depth, and enhances two-layered exchange flow. In summer, the wind stress in Ise Bay is generally < 0.02 N m^{-2}, and thus, the typical magnitude of the wind-driven current is < 0.6 cm s^{-1}. The maximum inflow velocity associated with the estuarine gravitational circulation in summer

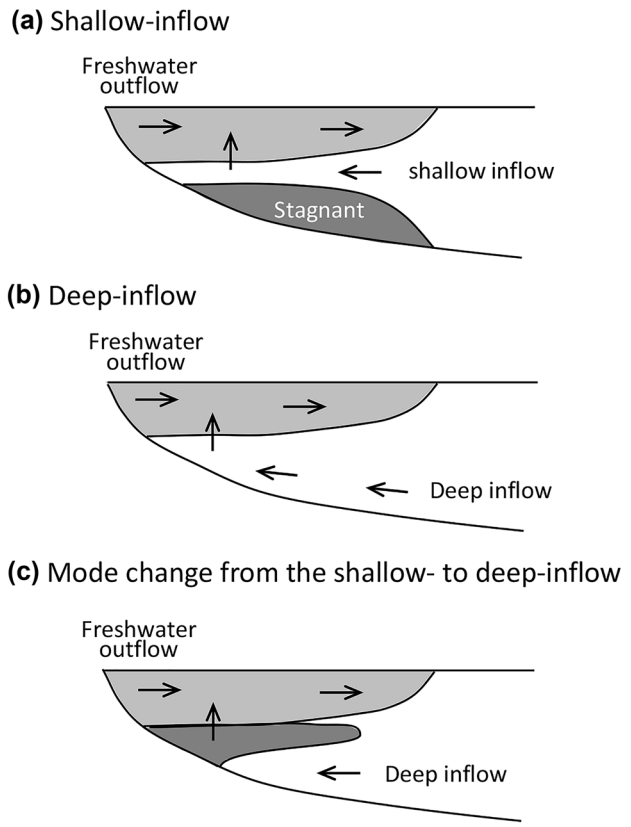

Fig. 9 Schematic diagram of the **a** shallow inflow, **b** deep inflow, and **c** phenomenon that occurs after the mode change from shallow to deep inflow

is > 8.0 cm s^{-1} (Fig. 6e). As such, the direct impact of the southwesterly wind on estuarine gravitational circulation in summer is insignificant. However, wind-induced mixing and straining can cause entrainment and changes in the estuarine gravitational flow (Valle-Levinson et al. 1998). The effect of wind on the inflow depth associated with estuarine gravitational flow in Ise Bay should be further examined in future studies.

There is freshwater input not only from the estuary head, but also from Mikawa Bay connected to Ise Bay (Fig. 1b), which could affect the strength of the surface outflow. In particular, the fresher water transported from Mikawa Bay possibly influences the density gradients between stations C5 and C9, which were used for estimating the driving force of the gravitational inflow (Fig. 7d). Slightly fresher water masses with a surface salinity of 0.5 lower than the salinity at 1 m depth were observed around station C7, such as in April 2010 (Fig. 4c). However, the influence of freshwater input from Mikawa Bay is not always clear throughout a year (Fig. 4c). This suggests that fresher water transported from Mikawa Bay may affect the density of the surface layer in Ise Bay, but does not affect the inflow in the lower layer at typical freshwater inputs (i.e., the annual mean discharge from Yahagi River to Mikawa Bay is 42 m^3 s^{-1}). The freshwater discharge from Mikawa Bay resulting from flood events and its influence on the inflow depth require further investigation.

The estuarine circulation in a wide estuary (e.g., Ise Bay) can be affected by Earth's rotation (Fujiwara et al. 1997). The effect of Earth's rotation on gravitational circulation is a laterally sheared flow (Valle-Levinson and Wilson 1998). In Ise Bay, density contour lines in cross-section slope to the left, suggesting a thermal wind distribution and that the inflow is concentrated at the lower right of the lateral section (Fujiwara et al. 1997). Moreover, the geomorphology of Irago Strait and Mikawa Bay may introduce curvature and lateral effects in the lower estuary and affect the inflow. Earth's rotation and geomorphology thus mainly influence the cross-sectional distribution of gravitational inflow throughout the year.

The bathymetry (i.e., from stations C1–7: Fig. 1b) could affect the stagnant bottom-waters and contribute to the thickness of the shallow inflow during the transition from deep to shallow waters (Fig. 9). In the central part of Ise Bay, station C6 (Fig. 1b) is about 2 m deeper than the other stations, such as station C7, and has a gentle depression-like topography (slope < 10^{-3}). For this reason, a cold bottom-water mass in summer tends to form near stations C5 and C6 at > 20 m depths (Fig. 4b). The thickness of the cold water mass, which is formed below the depth of the shallow inflow, is largest near station C6. However, the cold water mass does not only exist in the depressions. The depth of the shallow inflow (Fig. 9a) in summer rises and is much shallower than the depth of the depressions (Figs. 5b and 7b).

Impact of Changing Inflow Depth on DO and CO_2 Dynamics in the Estuary

The seasonal change in the inflow depth affects various functions of the estuary. In particular, the transition from the shallow inflow to the deep inflow (Fig. 9) facilitates the release of any materials that had been previously trapped and stored in the lower layer.

During the heating period, the water under the inflow layer becomes hypoxic, as shown in Fig. 4. The thickness of the low-DO layer (blue part) increases from April to July, in accord with the ascent of the inflow layer (Fig. 6). In contrast, the disappearance process of low-DO water masses propagates rapidly. The bottom low-DO water is frequently lifted up from the bottom and lost, rather than being eroded from above (Fig. 4). The cooling and DO ascension were both found first from the *bottom* during the cooling period in the estuary (Fig. 5e).

The progress of the hypoxia had been explained by the strength of the stratification which disturbed vertical oxygen

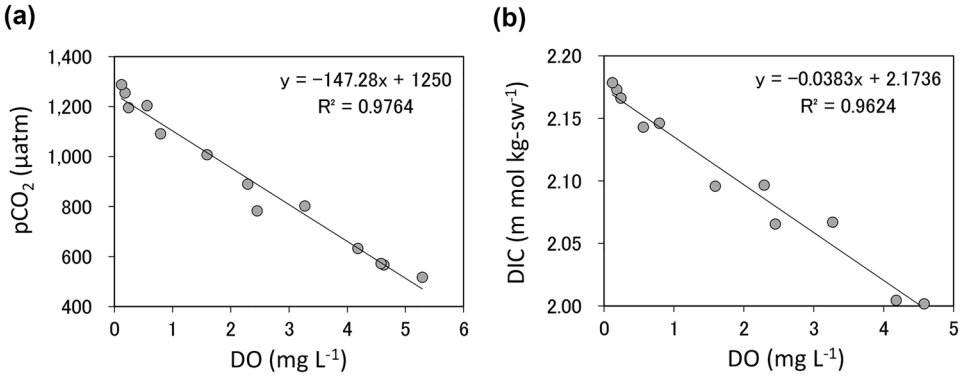

Fig. 10 Relationship between the **a** partial pressure of CO_2 and **b** dissolved inorganic carbon and DO in water 1 m above the seafloor in Ise Bay (July 2019)

supply in estuaries, like that in lakes. However, in the estuary, rapid disappearance of the hypoxia occurs in late October and November, even if over-turn does not happen at that time. In particular, the lateral process (especially inflow) has a large influence on the development and cessation of the hypoxia in estuaries, where salinity stratification covers the sea surface. This may be a difference of the estuarine hypoxia from hypoxia observed in lakes.

In this study, we have indicated that the generation, development, and disappearance of hypoxic water mass are closely related to the changing inflow depth. Below, we show that the hypoxic water contains a large amount of CO_2, which were generated by the mineralization of the organic matter sinking from the upper layer.

Figure 10 indicates a relationship between DO and pCO_2 and DIC in the lower layer water in Ise Bay in July 2019. DO is closely correlated to the partial pressure of CO_2 (pCO_2; $p = 0.001$: Fig. 10a). As pCO_2 in the air is approximately 400 µatm, the lower layer water contains excess CO_2 at all stations. Figure 10 b indicates that oxygen consumption of 1 mol corresponds to CO_2 generation of 1.2 mol. In this way, hypoxic water stores CO_2 and intermittently releases them to the upper layer, which may stimulate primary production. As the changing inflow depth plays an important role in oxygen dynamics, it is likely that the depth change also affects CO_2 dynamics in estuaries.

Conclusions

In this study, we used in situ current measurements and hydrographic surveys covering a period of 7 years to verify the seasonal changes in the depths of the seawater inflow associated with estuarine gravitational circulation. The preconditions that allow the seasonal changes to inflow depth to occur are as follows. (i) Although seawater density (σ) is generally governed by salinity (S) in estuaries, the temperature change ($\partial T/\partial t$) is the main contributor to seasonal change in density ($\partial\sigma/\partial t$) in the lower layer, where T is temperature, and t is time. (ii) In the lower layer, the temperature rises or falls faster in the lower half of the estuary than in the upper half of the estuary, because there is generally strong salinity stratification in the upper half of the estuary, and it prevents the heat transfer from the surface to the deeper waters. (iii) Spatial inhomogeneity in heating or cooling in the lower layer causes a horizontal density gradient in this layer, and this induces the mode change. These preconditions highlight the important role of temperature in estuarine dynamics, which has been somewhat ignored by previous studies.

The mechanism associated with the seasonal changes to the inflow mode can be summarized as follows.

– *Winter*: Deep inflow associated with a classical salinity-governed two-layer flow dominates.
– *Spring to summer (heating period)*: Transition from the deep to shallow inflow occurs.

  - The lower-estuary water becomes lighter than the upper-estuary water in the lower layer, via the mechanism described in precondition (ii), and this lifts the inflow upward and forms the shallow inflow.
  - As the bottom water beneath the shallow inflow is separated from the heat source, the temperature difference between the upper and lower estuary is enhanced (i.e., a positive feedback develops).

– *Fall to winter (cooling period)*: Reversal process occurs and returns to the deep inflow.
  - As the cooling proceeds faster in the lower estuary than in the upper estuary in the lower layer, a water mass that is at least 1 °C warmer than the water in the middle layer remains on the seabed in the upper estuary.

As the salinity stratification continues even in winter in estuaries, a full over-turn does not occur. Nevertheless, the hypoxic water mass disappears in winter in the majority of estuaries. This phenomenon can be satisfactorily explained

because the hypoxic water mass is washed away by the lateral inflow (the deep inflow in fall and winter). The occurrence, development, and disappearance of the hypoxic water mass is strongly affected by the change in inflow depth. In particular, the appearance of the middle-layer hypoxia in August, October, and November is a prominent example of this effect. In this way, the mode change plays a key role in oxygen dynamics in estuaries and nearshore coastal waters. As the hypoxic water contains a large amount of CO_2, this mode change also affects the CO_2 dynamics. The lateral flow plays an important role in oxygen and CO_2 dynamics in estuaries and nearshore coastal waters.

Acknowledgements We are grateful for the monitoring data provided and supplied by the Nagoya Research and Engineering Office for Port and Airport, Chubu Regional Development Bureau, Ministry of Land, Infrastructure, Transport and Tourism. The monthly hydrographic observations were downloaded from the home pages of the Hydrographic and Oceanographic Department, Japan Coast Guard, and Mie Prefecture Fisheries Research Institute.

References

Banas, N.S., B.M. Hickey, P. MacCready, and J.A. Newton. 2004. Dynamics of Willapa Bay Washington: A Highly Unsteady Partially Mixed Estuary. *Journal of Physical Oceanography* 34: 2413–2427. https://doi.org/10.1175/JPO2637.1.

Basdurak, N.B., and A. Valle-Levinson. 2012. Influence of Advective Accelerations on Estuarine Exchange at a Chesapeake Bay Tributary. *Journal of Physical Oceanography* 42 (10): 1617–1634. https://doi.org/10.1175/jpo-d-11-0134.1.

Belzile, M., P.S. Galbraith, and D. Bourgault. 2016. Water renewals in the Saguenay Fjord. *Journal of Geophysical Research: Oceans* 121: 638–657. https://doi.org/10.1002/2015JC011085.

Burchard, H., and R.D. Hetland. 2010. Quantifying the Contributions of Tidal Straining and Gravitational Circulation to Residual Circulation in Periodically Stratified Tidal Estuaries. *Journal of Physical Oceanography* 40 (6): 1243–1262. https://doi.org/10.1175/2010JPO4270.1.

Chant, R.J. 2002. Secondary circulation in a region of flow curvature: Relationship with tidal forcing and river discharge. *Journal of Geophysical Research: Oceans* 107: 3131. https://doi.org/10.1029/2001JC001082.

Chen, C.-T.A., and A.V. Borges. 2009. Reconciling opposing views on carbon cycling in the coastal ocean: Continental shelves as sinks and near-shore ecosystems as sources of atmospheric CO_2. *Deep Sea Research Part II: Topical Studies in Oceanography* 56: 578–590. https://doi.org/10.1016/j.dsr2.2009.01.001.

Chen, S.N., W.R. Geyer, D.K. Ralston, and J.A. Lerczak. 2012. Estuarine Exchange Flow Quantified with Isohaline Coordinates: Contrasting Long and Short Estuaries. *Journal of Physical Oceanography* 42 (5): 748–763. https://doi.org/10.1175/JPO-D-11-086.1.

Cheng, P., J. Mao, F. Yu, N. Chen, A. Wang, and F. Xu. 2019. A numerical study of residual flow induced by eddy viscosity-shear covariance in a tidally energetic estuary. *Estuarine Coastal and Shelf Science* 230: 106446. https://doi.org/10.1016/j.ecss.2019.106446.

Coastal Oceanography Research Committee. 1985. *Coastal Oceanography of Japanese Island*, ed. H. Kunishi. Tokyo: Tokai Univ Press.

Conroy, T., D.A. Sutherland, and D.K. Ralston. 2020. Estuarine Exchange Flow Variability in a Seasonal Segmented Estuary. *Journal of Physical Oceanography* 50 (3): 595–613. https://doi.org/10.1175/JPO-D-19-0108.1.

Dijkstra, Y.M., H.M. Schuttelaars, and H. Burchard. 2017. Generation of exchange flows in estuaries by tidal and gravitational eddy viscosity-shear covariance (ESCO). *Journal of Geophysical Research: Oceans* 122: 4217–4237. https://doi.org/10.1002/2016JC012379.

Dzwonkowski, B., P. Kyeong, H. Kyung, W.M. Graham, F.J. Hernandez, and S.P. Powers. 2011. Hydrographic variability on a coastal shelf directly influenced by estuarine outflow. *Continental Shelf Research* 31 (9): 939–950. https://doi.org/10.1016/j.csr.2011.03.001.

Fofonoff, N.P., and R.C. Millard Jr. 1983. Algorithms for Computation of Fundamental Properties of Seawater. *Unesco Technical Papers in Marine Science* 44: 1–53.

Fujii, T., T. Fujiwara, K. Sayashi, K. Yuasa, I. Noda, T. Ono, and T. Ishikawa. 2015. Generation mechanism of hypoxic water in the nearshore water overlaid with a river plume. *Journal of Japan Society of Civil Engineers B2 (Coastal Engineering)* 71: 1285–1290.

Fujiwara, T., L.P. Sanford, K. Nakatsuji, and Y. Sugiyama. 1997. Anticyclonic circulation driven by the estuarine circulation in a gulf type ROFI. *Journal of Marine Systems* 12: 83–99. https://doi.org/10.1016/S0924-7963(96)00090-5.

Fujiwara, T., T. Takahashi, A. Kasai, Y. Sugiyama, and M. Kuno. 2002. The role of circulation in the development of hypoxia in Ise Bay Japan. *Estuarine Coastal and Shelf Science* 54: 19–31. https://doi.org/10.1006/ecss.2001.0824.

Fujiwara, T., and Y. Yamada. 2002. Inflow of oceanic water into Tokyo Bay and generation of a subsurface hypoxic water mass. *Journal of Geophysical Research: Oceans* 107: 1–11. https://doi.org/10.1029/2000JC000749.

Geyer, W.R., and P. MacCready. 2014. The Estuarine Circulation. *Annual Review of Fluid Mechanics* 46: 175–197.

Giddings, S.N., and P. MacCready. 2017. Reverse Estuarine Circulation Due to Local and Remote Wind Forcing Enhanced by the Presence of Along-Coast Estuaries. *Journal of Geophysical Research: Oceans* 122: 10184–10205. https://doi.org/10.1002/2016JC012479.

Guo, X., and A. Valle-Levinson. 2007. Tidal effects on estuarine circulation and outflow plume in the Chesapeake Bay. *Continental Shelf Research* 27 (1): 20–42. https://doi.org/10.1016/j.csr.2006.08.009.

Hansen, D.V., and M. Rattray. 1966. New dimensions in estuary classification. *Limnology and Oceanography* 11: 319–325. https://doi.org/10.4319/lo.1966.11.3.0319.

Hickey, B.M. 2002. Coupling between the California Current System and a coastal plain estuary in low riverflow conditions. *Journal of Geophysical Research: Oceans* 107 (C10): 3166. https://doi.org/10.1029/1999JC000160.

Hill, A.E. 1993. Seasonal gyres in shelf seas. *Annales Geophysicae* 11: 1130–1137.

Houghton, R.W., R. Schlitz, R.C. Beardsley, B. Butman, and J.L. Chamberlin. 1982. The middle Atlantic Bight cold pool: Evolution of the temperature structure during summer 1979. *Journal of Physical Oceanography* 12: 1019–1029.

Kobayashi, S., H. Zenitani, K. Nagamoto, A. Futamura, and T. Fujiwara. 2010. Gravitational circulation and its response to the variation in river discharge in the Seto Inland Sea Japan. *Journal of Geophysical Research: Oceans* 115(C03009). https://doi.org/10.1029/2007JC004503

Large, W.G., and S. Pond. 1981. Open ocean momentum flux measurements in moderate to strong winds. *Journal of Physical Oceanography* 11: 324–336. https://doi.org/10.1175/1520-0485(1981)011.

Lerczak, J.A., and W.R. Geyer. 2004. Modeling the lateral circulation in straight stratified estuaries. *Journal of Physical Oceanography* 34 (6): 1410–1428. https://doi.org/10.1175/1520-0485.

Lewis, E. and D. W. R. Wallace. 1998. *Program Developed for CO_2 System Calculations ORNL/CDIAC-105*. Oak Ridge: Carbon Dioxide Information Analysis Center.

MacCready, P. 2011. Calculating Estuarine Exchange Flow Using Isohaline Coordinates. *Journal of Physical Oceanography* 41 (6): 1116–1124.

MacCready, P., W.R. Geyer, and H. Burchard. 2018. Estuarine Exchange Flow is Related to Mixing through the Salinity Variance Budget. *Journal of Physical Oceanography* 48 (6): 1375–1384.

Nakajima, M., and T. Fujiwara. 2007. Estuarine Circulation and Hypoxic Water Mass in Osaka Bay. *Bulletin on Coastal Oceanography* 44 (2): 157–163.

Nidzieko, N.J., and S.G. Monismith. 2013. Contrasting Seasonal and Fortnightly Variations in the Circulation of a Seasonally Inverse Estuary Elkhorn Slough California. *Estuaries and Coasts* 36 (1): 1–17. https://doi.org/10.1007/s12237-012-9548-1.

Pritchard, D.W. 1952. Salinity distribution and circulation in the Chesapeake Bay estuarine system. *Journal of Marine Research* 11 (2): 106–123.

Pritchard, D.W. 1956. The dynamic structure of a coastal plain estuary. *Journal of Marine Research* 15: 33–42.

Reyes-Hernandez, A.C., and A. Valle-Levinson. 2010. Wind Modifications to Density-Driven Flows in Semienclosed Rotating Basins. *Journal of Physical Oceanography* 40 (7): 1473–1487. https://doi.org/10.1175/2010JPO4230.1.

Shearman, R.K., and K.H. Brink. 2010. Evaporative dense water formation and cross-shelf exchange over the northwest Australian inner shelf. *Journal of Geophysical Research: Oceans* 115: C06027. https://doi.org/10.1029/2009JC005931.

Stigebrandt, A., and O. Kalén. 2013. Improving Oxygen Conditions in the Deeper Parts of Bornholm Sea by Pumped Injection of Winter Water. *Ambio* 42: 587–595.

Taguchi, F., and T. Fujiwara. 2010. Carbon dioxide stored and acidified low oxygen bottom waters in coastal sea Japan. *Estuarine Coastal and Shelf Science* 86: 429–433. https://doi.org/10.1016/j.ecss.2009.07.037.

Thomson, R.E., S.F. Mihály, and E.A. Kulikov. 2007. Estuarine versus transient flow regimes in Juan de Fuca Strait. *Journal of Geophysical Research: Oceans* 112: 1–25. https://doi.org/10.1029/2006JC003925.

URL1: http://www1.river.go.jp/

URL2: http://www.data.jma.go.jp/kaiyou/db/tide/suisan/station.php

URL3: https://www1.kaiho.mlit.go.jp/KAN4/kaisyo/isewan/isewan_kankyo.html

URL4: https://www.pref.mie.lg.jp/suigi/hp/000050873.htm

URL5: http://www.isewan-db.go.jp/real_web/REAL_WEB_buoy/PointSelect/Index

URL6: http://www.data.jma.go.jp/obd/stats/etrn/index.php

Valle-Levinson, A., C. Li, T.C. Royer, and L.P. Atkinson. 1998. Flow patterns at the Chesapeake Bay entrance. *Continental Shelf Research* 18: 1157–1177.

Valle-Levinson, A., and R.E. Wilson. 1998. Rotation and vertical mixing effects on volume exchange in eastern Long Island Sound. *Estuarine Costal and Shelf Science* 46: 573–585.

Valle-Levinson, A. 2011. Classification of Estuarine Circulation. In *Treatise on Estuarine and Coastal Science*, vol. 1, ed. E. Wolanski and D.S. McLusky, 75–86. Waltham: Academic Press.

Wang, T., and W.R. Geyer. 2018. The Balance of Salinity Variance in a Partially Stratified Estuary: Implications for Exchange Flow Mixing and Stratification. *Journal of Physical Oceanography* 48 (12): 2887–2899. https://doi.org/10.1175/JPO-D-18-0032.1.

Wong, K.-C. 1994. On the nature of transverse variability in a coastal plain estuary. *Journal of Geophysical Research: Oceans* 99: 14209–14222.